J. Fluid Mech. (1996), vol. 324, pp. 1–23

Higher-order resonant instabilities of internal gravity waves

By L. J. SONMOR[1]† AND G. P. KLAASSEN[2]

[1] Institute of Space and Atmospheric Studies, University of Saskatchewan, Saskatoon, Saskatchewan, Canada S7N 5E2

[2] Department of Earth and Atmospheric Science, York University, North York, Ontario, Canada M3J 1P3

(Received 15 August 1994 and in revised form 4 April 1996)

We investigate the three-dimensional characteristics of a general class of resonant temporal instabilities of internal gravity waves, in which the disturbance comprises two infinitesimal internal gravity waves satisfying the conditions $\omega_I+\omega_{II}=n\tilde{\omega}$, $\boldsymbol{k}_I+\boldsymbol{k}_{II}=n\tilde{\boldsymbol{k}}$, with growth rates of order $N(|\tilde{\boldsymbol{u}}|\,|\tilde{\boldsymbol{k}}|/N)^n$, assuming small dimensional primary-wave velocity amplitude $|\tilde{\boldsymbol{u}}|$. We derive simple equations for their wavenumbers, frequency, growth rate, and energy budget. Interactions involving more than two disturbance components are shown not to represent distinct families of solutions, but rather to comprise order transitions linking together two or more 'two-disturbance-component' solutions of different order n. Unlike $n=1$ resonant instabilities, those with $n\geqslant 3$ can align with the wave shear flow. We calculate the peak growth rate, spanwise wavenumber, and energy budget of shear-aligned resonance, as functions of wave frequency; they extract energy from both the wave shear and buoyancy fields.

1. Introduction

Recent simulations (Winters & D'Asaro 1994; Fritts, Isler & Andreassen 1994) and observations (Fritts, Isler & Thomas 1993) of large-amplitude internal gravity waves have highlighted the importance of shear-aligned instabilities. These results would seem to be in accordance with a wealth of evidence that in a variety of flows convective instabilities often take the form of shear-aligned rolls (Kelly 1977; Clever & Busse 1977; Klaassen & Peltier 1985, 1991; McIntyre 1989). An internal gravity wave comprises a non-horizontal, oscillating, stratified, parallel shear flow which permits shear-aligned orientation of secondary instability even in the absence of background shear. Indeed, Thorpe (1994) found shear-aligned linear instability to dominate for the vertical profiles associated with a moderately overturned zero-frequency wave in a static background.

Small-amplitude waves are subject to resonant instabilities (Phillips 1960, 1966), the most familiar of which comprise pairs of waves (denoted I and II) whose frequencies ω and wavenumbers $\boldsymbol{k}$ are related to those of the primary wave (denoted with a tilde) through the condition $\omega_I+\omega_{II}=\tilde{\omega}, \boldsymbol{k}_I+\boldsymbol{k}_{II}=\tilde{\boldsymbol{k}}$. Each disturbance wavenumber of these lowest-order resonances must have a component parallel to the primary-wave parcel motions, thus excluding the possibility of shear-aligned instability. As we shall demonstrate, higher-order resonances do not share this exclusion. Hasselmann (1967) discussed the existence of a higher-order interaction satisfying $\omega_I+\omega_{II}=2\tilde{\omega}$,

---

† Present address: Department of Earth and Atmospheric Sciences, York University, North York, Ontario, Canada.

$\boldsymbol{k}_I + \boldsymbol{k}_{II} = 2\tilde{\boldsymbol{k}}$. He showed that it obeys the same stability criterion as its lower-order counterpart, but did not derive an equation for the instability growth rate. Higher-order resonances are of particular importance for surface gravity waves, since the $n = 2$ solution obtained by Zakharov (1968) is the lowest-order resonance for this type of primary-wave motion, i.e. no $n = 1$ solution exists. Zakharov also mentioned the existence of an infinite set of resonances satisfying $\omega_I + \omega_{II} = n\tilde{\omega}, \boldsymbol{k}_I + \boldsymbol{k}_{II} = n\tilde{\boldsymbol{k}}$, with $n = 3, 4, \dots, \infty$, but did not derive detailed properties. McLean (1982) presented finite-amplitude numerical results that support Zakharov's claim that for small primary-wave amplitude, the growth rate scales with the nth power of that amplitude. Drazin (1977) found the same scaling for internal-wave resonance.

This growth-rate scaling has generally been interpreted to mean that higher-order resonances of internal waves are unimportant, because $n = 1$ resonance must dominate when the wave amplitude is small. However, it also allows the possibility that the growth rate of a higher-order resonance might exceed that of lower-order resonances at finite primary-wave amplitude, and so become physically observable. A recent study by the present authors (manuscript in preparation) of linear instability of finite-amplitude gravity waves suggests that this is indeed the case. At large wave amplitude, they found growing shear-aligned instability whose characteristics agree with those found in recent studies of steady vertical profiles by Thorpe (1994) and Winters & Riley (1992). Figure 1 illustrates the growth rate of a shear-aligned instability as a function of wave amplitude for a (propagating) wave with a non-vertical phase elevation angle. At amplitudes for which the wave has overturned, the growth rate is very large – on the order of the Brunt–Väisälä frequency. As the wave amplitude is decreased, the continuously evolving solution exhibits remarkable behaviour not found for strictly vertical profiles. Rather than vanishing at a finite amplitude, the growth rate approaches zero with a simple $+5$ power-law dependence. Inspection of the solution structure at small amplitude reveals two dominant components which satisfy the $n = 5$ higher-order resonant relations. (Other orders n of shear-aligned instability dominate in other regions of wave parameter space.) Figure 1 also shows that this $n = 5$ instability overtakes the $n = 1$ parametric subharmonic instability at a wave amplitude just beyond the critical overturning value. This behaviour suggests that higher-order resonant instabilities are more relevant than has often been assumed. It prompted us to investigate in this paper their detailed nature at small wave amplitude, in the expectation that these simplified characteristics will improve our understanding of shear-aligned instabilities of large-amplitude waves.

Many previous treatments of resonant interactions have utilized weakly nonlinear analysis, in which all wave components have comparable amplitudes. However, Mied (1976), Drazin (1977), and Klostermeyer (1982) showed that a linear stability analysis of a finite-amplitude primary wave is sufficient to characterize resonant instabilities. Indeed some analyses which begin with a weakly nonlinear formulation of resonances eventually resort to linearization (e.g. Hasselmann 1967; Yeh & Liu 1981). Although the weakly nonlinear approach is powerful, higher-order theory becomes progressively more difficult to formulate. A linear formulation will allow us to derive equations that apply to arbitrary orders of resonance, for the restricted set of interactions in which one component dominates.

Mied (1976) and Klostermeyer (1982) used Floquet analyses to derive two-dimensional equations describing linear instabilities of finite-amplitude gravity waves, and solved them for selected values of wave amplitude and frequency. Drazin (1977) used a different Floquet formalism to derive three-dimensional equations describing a different type of gravity-wave instability. He expanded the two-

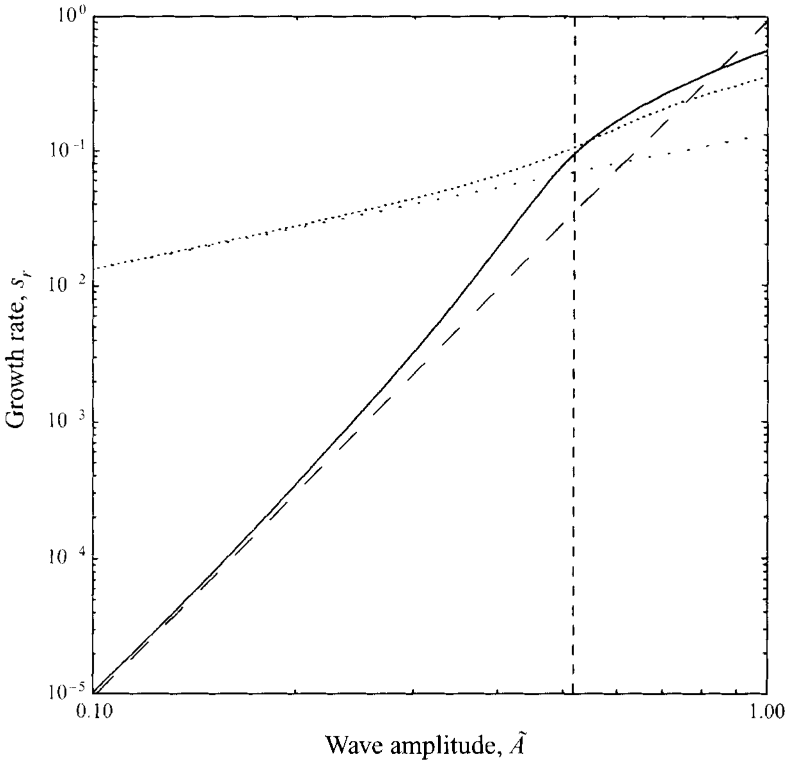

FIGURE 1. The solid line gives the growth rate (in units of Brunt–Väisälä frequency N) of a shear-aligned instability versus wave amplitude $\tilde{A}$, for a propagating gravity wave with phase elevation angle $\theta = 75°$. The vertical dashed line marks the critical amplitude for vertical overturning. The line with long dashes is an extrapolation of the small-$\tilde{A}$ dependence (slope 5). For comparison, the growth rate of two-dimensional $n = 1$ parametric subharmonic instability (PSI) is also shown (densely dotted line) for the same finite-$\tilde{A}$ wave. The line with slope 1 (sparse dots) extrapolates the small-$\tilde{A}$ asymptotic growth rate of PSI.

dimensional form of these equations in powers of primary-wave amplitude to investigate resonant instabilities of small-amplitude waves, and included a short qualitative discussion of higher-order resonances. As noted by Drazin, it is not always feasible to relate his modes of instability to those obtained by Mied and Klostermeyer. Whereas the latter's equations describe temporal instability, in which a disturbance grows in time while remaining bounded in space, Drazin's equations describe a different type of instability, in which a disturbance grows with primary-wave phase. Thus, on a plane of constant phase, the unstable modes calculated by Drazin do not grow in time, in contrast to the temporally growing modes we wish to consider.

In §2 we apply the equations of Mied and Klostermeyer to three-dimensional disturbances, and expand the solution in powers of primary-wave amplitude. Section 3 gives the disturbance wavenumber and frequency relations. We derive equations for the instability growth rate and energy budget in §4. We also present numerical results illustrating the three-dimensional properties of resonant instabilities (§5), a discussion of instabilities comprising more than two disturbance components (§6), and, in §7, an investigation of shear-aligned higher-order resonant instabilities.

2. Floquet analysis of temporal instabilities of internal gravity waves

Consider a monochromatic finite-amplitude internal gravity wave with phase elevation angle θ, as sketched in figure 2. Taking the y-axis perpendicular to the plane of wave oscillation and propagation, we introduce rotated coordinates ξ and η that are respectively perpendicular and parallel to the wavenumber vector. Assuming an inviscid, non-rotating uniform-Brunt–Väisälä-frequency fluid, the scaled Boussinesq equations governing an infinitesimal disturbance are

$$\partial_t u+\tilde{u}\partial_\xi u+(\partial_\eta \tilde{u})\, w+\partial_\xi p+b\cos\theta = 0, \tag{1a}$$

$$\partial_t v+\tilde{u}\partial_\xi v+\partial_y p = 0, \tag{1b}$$

$$\partial_t w+\tilde{u}\partial_\xi w+\partial_\eta p-b\sin\theta = 0, \tag{1c}$$

$$\partial_t b+\tilde{u}\partial_\xi b+(\partial_\eta \tilde{b})\, w-u\cos\theta+w\sin\theta = 0, \tag{1d}$$

$$\partial_\xi u+\partial_y v+\partial_\eta w = 0, \tag{1e}$$

where $\boldsymbol{u} = u\hat{\boldsymbol{e}}_\xi+v\hat{\boldsymbol{e}}_y+w\hat{\boldsymbol{e}}_\eta$ is the disturbance velocity, b is the disturbance buoyancy, p is the disturbance pressure, and a tilde denotes a primary-wave quantity. The time and distance scales used are the inverse of the Brunt–Väisälä frequency N and the inverse of the magnitude of the dimensional wavenumber $\tilde{\boldsymbol{k}}_d$ of the primary wave. The dimensionless primary-wave quantities may be written as

$$\tilde{u} = -2\tilde{A}\sin\phi, \quad \tilde{b} = -2\tilde{A}\cos\phi, \quad \phi = \eta-\tilde{\omega}t, \quad \tilde{\omega} = \cos\theta, \tag{2}$$

where $\tilde{A}$ is the dimensionless amplitude of the primary wave. The neglect of rotation restricts the direct application of the results to gravity waves with phase elevation angles not too near vertical. The neglect of products of disturbance quantities restricts the analysis to disturbances that are infinitesimal relative to the primary-wave amplitude, i.e. if the dimensionless disturbance velocity scale (relative to $N/|\tilde{\boldsymbol{k}}_d|$) is ϵ, then

$$\epsilon \ll \tilde{A}. \tag{3}$$

The linearity of (1) and the sinusoidal nature of the primary-wave coefficients entail a general form of solution prescribed by Floquet theory. Defining a dynamic variable vector

$$\boldsymbol{D} \equiv (u, v, w, b, p)^T, \tag{4}$$

the solution can be written as

$$\boldsymbol{D} = \mathrm{e}^{st+\mathrm{i}(\kappa\xi+\lambda y+\mu\phi)} \sum_{m=-\infty}^{\infty} \boldsymbol{D}_m \mathrm{e}^{\mathrm{i}m\phi}, \tag{5}$$

where s is a complex coefficient comprising the disturbance growth rate s_r and relative frequency s_i (observed from fixed primary-wave phase), κ and λ are the real ξ and y disturbance wavenumbers, μ is the real Floquet parameter that determines the modulation of the disturbance relative to the primary wave period (i.e. if μ can be written as a rational number, then the modulation period is the primary-wave period multiplied by the lowest denominator). The linearity of (1) leaves $\boldsymbol{D}$ undetermined to a multiplicative scalar coefficient, whose order is ϵ by assumption. Equivalent forms of solution have been used by Mied (1976) and Klostermeyer (1982) to investigate two-dimensional disturbances of internal gravity waves; McLean (1982) used a similar form to investigate the stability of finite-amplitude surface waves. As noted in the introduction, Drazin (1977) used a different Floquet formulation. In our notation, he imposed imaginary s and solved for complex μ, yielding solutions with non-zero $\mathrm{Im}(\mu)$

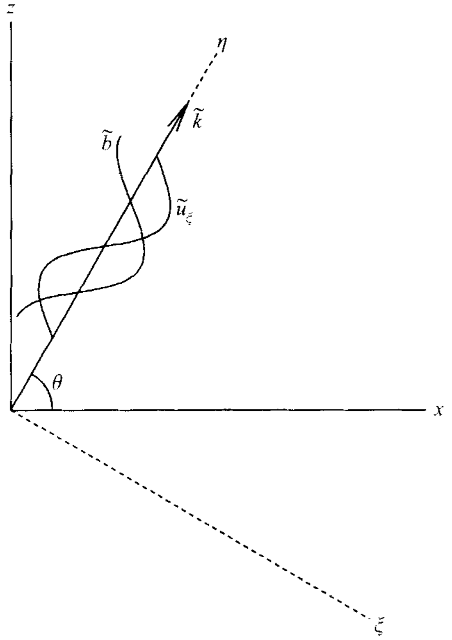

FIGURE 2. Orientation of our coordinate system, and schematic of the phase relation of the primary wave fields.

which grow in wave phase. Our treatment imposes real μ and solves for complex s, yielding temporally unstable solutions with positive Re(s) (Re and Im denote real and imaginary parts).

Our analysis departs from that of Mied and Klostermeyer in that it assumes small primary-wave amplitude $\tilde{A}$ (but always $\tilde{A} \gg \epsilon$), and expands s and $\boldsymbol{D}_m$ in powers of $\tilde{A}$:

$$\boldsymbol{D}_m = \epsilon \sum_{j=0}^{\infty} \boldsymbol{D}_m^{(j)} \tilde{A}_j, \quad s = \sum_{j=0}^{\infty} s^{(j)} \tilde{A}_j. \tag{6}$$

With the form assumed above, the perturbation coefficients $s^{(j)}$ and $\boldsymbol{D}_m^{(j)}$ are $O(1)$. It is valid to investigate the solution of the linearized disturbance equations to arbitrary order in primary-wave amplitude $\tilde{A}$, say $\tilde{A}^J$, as long as the disturbance velocity scale is much smaller (i.e. $\epsilon \ll \tilde{A}^J$), because the terms ignored in the linearization (equation (1)) are $O(\epsilon^2)$, and the smallest investigated terms are then $O(\epsilon \tilde{A}^J)$. We will examine the solutions in the three-dimensional disturbance wavenumber space (κ, λ, μ).

We will also use solutions of the finite-$\tilde{A}$ equations, (1), at small $\tilde{A}$ to verify the results obtained using the above power-series technique. These solutions are obtained from the eigenvalue equations that result when the Floquet form of solution (equation (5)) is substituted into (1), and the Floquet sum is truncated suitably. Our finite-$\tilde{A}$ method is directly analogous to that used by Klostermeyer (1982) for two-dimensional disturbances. Upon specification of $\tilde{A}$, θ, κ, λ, and μ, the eigenvalue equation is solved to find all the growing solutions, using standard EISPACK software for obtaining matrix eigenvalues (s) and eigenvectors ($\boldsymbol{D}_m$). For the small $\tilde{A}$ values used here, the required truncations are quite modest (i.e. no more severe than $-10 \leqslant m \leqslant 10$).

3. Disturbance wavenumbers and frequencies

Small-$\tilde{A}$ theory of resonant interactions requires an assumption regarding the number of leading-order ($O(\epsilon)$) disturbance components that participate in the interaction; this is equivalent to the number of non-vanishing coefficients $\boldsymbol{D}_m$ in the Floquet expansion (5) in the limit $\tilde{A} \rightarrow 0$ (but always $\tilde{A} \gg \epsilon$). We refer to this number as M. In §§3–5, we consider only resonant interactions of the form $M = 2$, as is conventional in weakly nonlinear analyses. The resulting interactions will involve the finite-amplitude primary wave plus two infinitesimal disturbance components in the limit $\tilde{A} \rightarrow 0$; for small but finite $\tilde{A}$, higher-order disturbance components also contribute, and are included in our analysis. Solutions involving only one $O(\epsilon)$ disturbance component ($M = 1$) do not exist for $\tilde{A} \rightarrow 0$. The existence and interpretation of solutions involving more than two $O(\epsilon)$ disturbance components ($M > 2$) will be investigated in §6.

The general solution (5) of equation (1) is invariant under the transformation

$$\mu \rightarrow \mu + m', \quad \boldsymbol{D}_m \rightarrow \boldsymbol{D}_{m-m'}, \quad m' \in I. \tag{7}$$

It follows that there exists a countably infinite set of identical solutions, or echoes, each shifted from its neighbour by 1 in the μ-direction. This symmetry allows us, without loss of generality, to set the index of one of the two $O(\epsilon)$ components to $m = 0$. We denote the other as $m = -n$, where n is the index separation of the two dominant disturbance components.

The leading-order ($O(\epsilon)$) disturbance solution is obtained by setting $\tilde{A} = 0$ (i.e. $\tilde{u} = \tilde{b} = 0$) in (1) and (6). This uncouples the two disturbance components; each must independently and simultaneously satisfy the same equations that govern the primary wave. Because of this $s^{(0)}$ is purely imaginary [$= \mathrm{i}s_i^{(0)}$]. Thus, in the limit $\tilde{A} \rightarrow 0$, the three components are all freely propagating waves.

The resonant condition follows immediately from the Floquet form of solution (equation (5)), which we convert to the wave form $\exp[\mathrm{i}(\boldsymbol{k} \cdot \boldsymbol{x} - \omega t)]$, with ω assumed non-negative. Let the imaginary time coefficients in the Floquet solution (5) (including that contained in ϕ) for the two disturbance waves in the limit $\tilde{A} \rightarrow 0$ be designated Ω_0 and Ω_{-n}, where

$$\Omega_m = s_i^{(0)} - (\mu + m)\,\tilde{\omega}. \tag{8}$$

There are three relevant cases, according to the signs of these two quantities:

case 1: $\Omega_0 > 0, \Omega_{-n} > 0$

$$\left.\begin{aligned} \omega_I &= s_i^{(0)} - \mu\tilde{\omega}, & \boldsymbol{k}_I &= (-\kappa, -\lambda, -\mu), \\ \omega_{II} &= s_i^{(0)} - (\mu - n)\,\tilde{\omega}, & \boldsymbol{k}_{II} &= (-\kappa, -\lambda, -\mu + n), \\ \omega_{II} - \omega_I &= n\tilde{\omega}, & \boldsymbol{k}_{II} - \boldsymbol{k}_I &= n\tilde{\boldsymbol{k}}; \end{aligned}\right\} \tag{9a}$$

case 2: $\Omega_0 < 0$, $\Omega_{-n} < 0$

$$\left.\begin{aligned} \omega_I &= -s_i^{(0)} + \mu\tilde{\omega}, & \boldsymbol{k}_I &= (\kappa, \lambda, \mu), \\ \omega_{II} &= -s_i^{(0)} + (\mu - n)\,\tilde{\omega}, & \boldsymbol{k}_{II} &= (\kappa, \lambda, \mu - n), \\ \omega_I - \omega_{II} &= n\tilde{\omega}, & \boldsymbol{k}_I - \boldsymbol{k}_{II} &= n\tilde{\boldsymbol{k}}; \end{aligned}\right\} \tag{9b}$$

case 3: $\Omega_0 \leqslant 0, \Omega_{-n} \geqslant 0$

$$\left.\begin{aligned} \omega_I &= -s_i^{(0)}+\mu\tilde{\omega}, & \boldsymbol{k}_I &= (\kappa,\lambda,\mu),\\ \omega_{II} &= s_i^{(0)}-(\mu-n)\,\tilde{\omega}, & \boldsymbol{k}_{II} &= (-\kappa,-\lambda,-\mu+n),\\ \omega_I+\omega_{II} &= n\tilde{\omega}, & \boldsymbol{k}_I+\boldsymbol{k}_{II} &= n\tilde{\boldsymbol{k}}, \end{aligned}\right\} \tag{9c}$$

where I and II denote the two dominant ($O(\epsilon)$) disturbance components, and we have used, according to our scaling, $\tilde{\boldsymbol{k}} = \hat{\boldsymbol{e}}_\eta$, the unit vector in the η-direction. The first two cases are referred to as difference interactions. Just as $n = 1$ difference interactions are neutrally stable, so are higher-order difference interactions (Hasselmann 1967). Our finite-$\tilde{A}$ numerical solutions confirm that difference interactions remain neutrally stable as the primary-wave amplitude increases, and hence do not appear to be physically important. The third case above is referred to as a sum interaction; in this type of interaction the two disturbance waves grow at the expense of the primary wave. The right-hand side of (9*c*) shows that the index separation n of the two dominant Floquet disturbance elements determines how many times the primary wave participates in the interaction.

For $n = 1$, we recover the triad interactions of Phillips (1960). For $n = 2$, we recover the higher-order interaction discussed by Hasselmann (1967). For $n > 2$, we recover an infinite set of higher-order interactions similar to those discussed by Drazin (1977), and by Zakharov (1968) in relation to surface gravity waves. It is tempting to refer to the interactions satisfying (9) as 'order-n resonant triads' because they involve one primary wave plus two disturbance components, or three waves in all. However, this would be inconsistent with previous usage (e.g. Hasselmann 1967; Craik 1985), in which these interactions are referred to as $(n+2)$-wave interactions in which the primary wave participates n times. For clarity and consistency, we classify resonant instabilities using two integers: n, the number of times the primary wave participates, and M, the number of $O(\epsilon)$ disturbance-wave components ($M = 2$ here).

Each of the two disturbance waves must satisfy the dispersion relation of the uncoupled equations that result from substitution of $\tilde{A} = 0$ into (1). For disturbances comprising two gravity waves (see Appendix A for disturbances involving vortical or acoustic modes), the relevant dispersion relations can be written as follows:

$$\omega_I = \left(\frac{[\mu\cos\theta+\kappa\sin\theta]^2+\lambda^2}{\mu^2+\kappa^2+\lambda^2}\right)^{1/2}, \quad \omega_{II} = \left(\frac{[(\mu-n)\cos\theta+\kappa\sin\theta]^2+\lambda^2}{(\mu-n)^2+\kappa^2+\lambda^2}\right)^{1/2}. \tag{10}$$

Substitution of (10) into the resonant-sum frequency condition of (9*c*) yields an equation in κ, λ, μ that governs the set of frequencies and wavenumbers of the disturbance waves for which the resonant-sum conditions are satisfied:

$$F_{sum} = \left(\frac{[\mu\cos\theta+\kappa\sin\theta]^2+\lambda^2}{\mu^2+\kappa^2+\lambda^2}\right)^{1/2} + \left(\frac{[(\mu-n)\cos\theta+\kappa\sin\theta]^2+\lambda^2}{(\mu-n)^2+\kappa^2+\lambda^2}\right)^{1/2} - n\tilde{\omega} = 0. \tag{11}$$

For fixed n and θ, the solution of (11) represents a two-dimensional surface in $(\kappa,\lambda,\mu) = \boldsymbol{k}_I$ space (i.e. $k_\eta = \mu$ for the $m = 0$ component). Then (10) yields ω_I and ω_{II} corresponding to any point on this $M = 2$ resonant-sum-interaction surface. Since $\omega_I \leqslant 1$ and $\omega_{II} \leqslant 1$, no solution exists for $\tilde{\omega} > 2/n$; equation (2) yields the Boussinesq restriction

$$\theta \geqslant \cos^{-1}(2/n) \tag{12}$$

for the presence of higher-order resonant instability with $n > 2$.

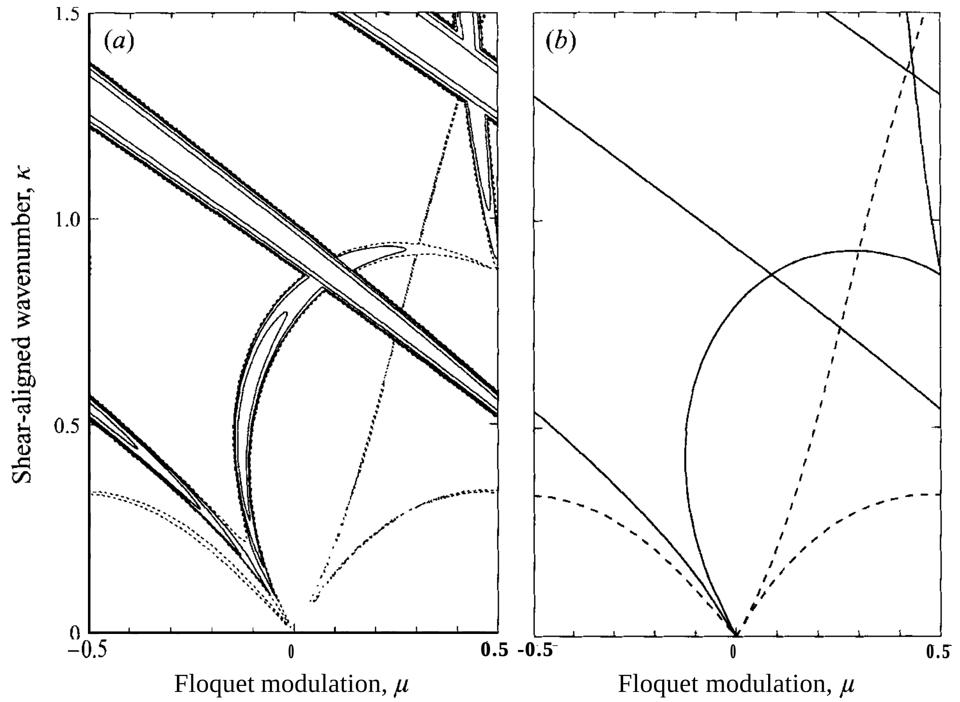

Figure 3. Existence of higher-order resonant solutions of the two-dimensional equations. Finite-A” growth-rate contours (a), with $\tilde{A} = 0.02$, $\theta = 30°$, $\lambda = 0$, are compared with $\lambda = 0$ cuts (*b*) of $n = 1$ (solid) and 2 (dashed) resonant surfaces and their echoes.

The $O(\epsilon)$ equations ((1), (2) with $\tilde{A} = 0$)) also yield a polarization relation for each of the two $O(\epsilon)$ disturbance internal gravity waves, giving the solution at this order:

$$D_\theta^{(0)} = P_0, \quad D_{-n}^{(0)} = rP_{-n}, \tag{13a, b}$$

$$P_m = \begin{pmatrix} \kappa\Omega_m^2 - \kappa\sin^2\theta - (\mu+m)\sin\theta\cos\theta \\ \lambda(\Omega_m^2 - 1) \\ (\mu+m)\,\Omega_m^2 - \kappa\sin\theta\cos\theta - (\mu+m)\cos^2\theta \\ \mathrm{i}\Omega_m[(\mu+m)\sin\theta - \kappa\cos\theta] \\ \Omega_m - \Omega_m^3 \end{pmatrix}, \tag{13c}$$

where Ω_m is given by (8), and r is the ratio of disturbance wave amplitudes; the overall arbitrary multiplier is included in ϵ in (6). The ratio of amplitudes r is not given by the $O(\epsilon)$ analysis, because the two disturbance components are uncoupled to O(e); it is fixed at $O(\epsilon A^n)$, as is shown in $4.

Figure 3 demonstrates that Mied’s (1976) and Klostermeyer’s (1982) two-dimensional equations possess solutions representing higher-order resonances. Figure *3(a)* shows growth-rate contours of the fastest-growing mode over two-dimensional disturbance-wavenumber (κ, μ) space, from finite-A˜solutions obtained over a fine grid, with fixed $\tilde{A} = 0.02$, $\theta = 30°$, $\lambda = 0$. The method used to obtain these solutions is described at the end of §2. Comparison with figure *3(b)* reveals that the positions of the contour ridgetops agree well with the $\lambda = 0$ cross-sections of the $n = 1$ and $n = 2$ resonant surfaces obtained from (1 1), and their echoes. The ‘fading out’ of the $n = 2$ contours in figure *3(a)* where they approach the $\kappa = \lambda = 0$ axis is due to the inability of finite grid spacing to resolve the extremely narrow $n = 2$ resonance. Note that $n > 2$ resonances involving only gravity waves do not exist for $\theta = 30$” (equation (12)).

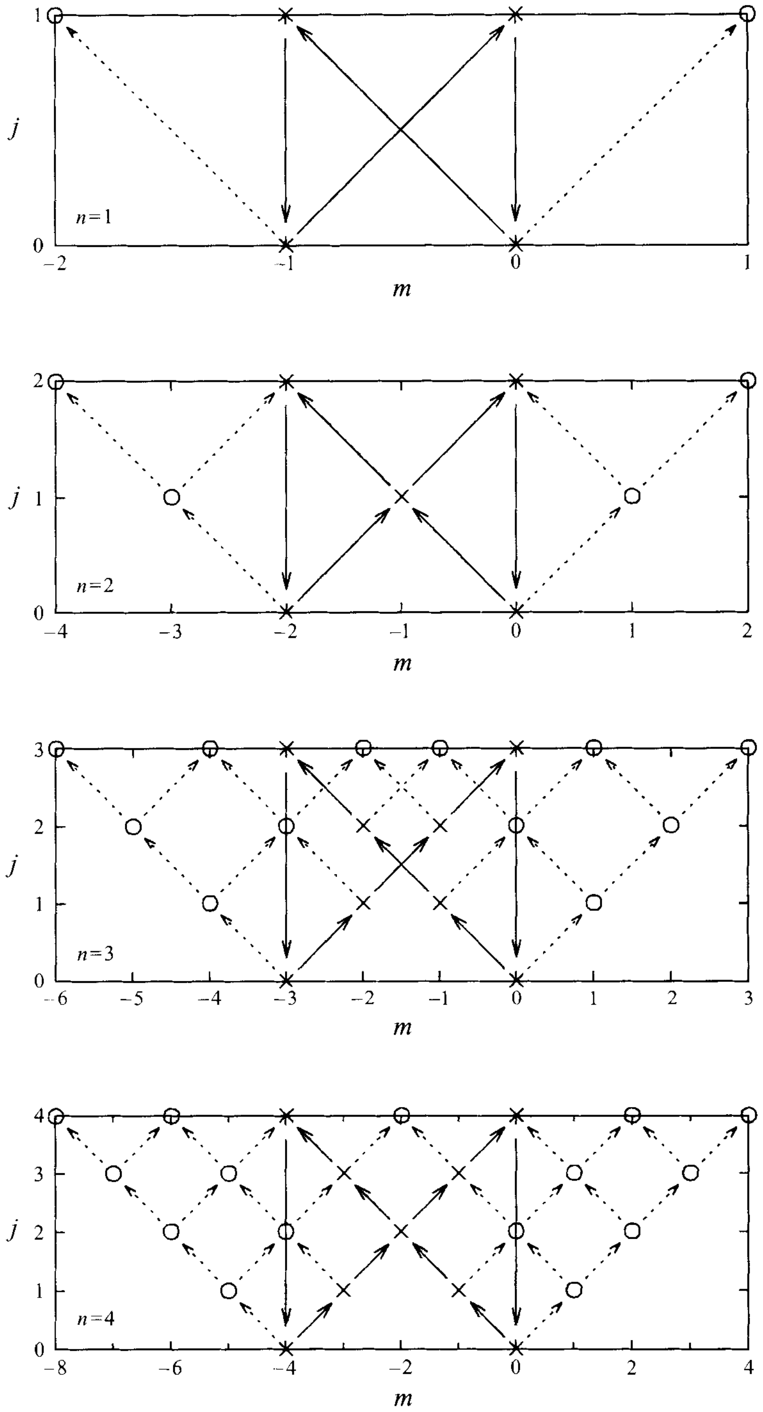

FIGURE 4. Coupling between Floquet-element coefficients $D_m^{(j)}$ (equations (5), (6)), for the first four resonant orders n, under the $M = 2$ assumption. Diagonal arrows indicate primary-wave couplings via $\tilde{u}$ and $\tilde{b}$ in (1), while vertical arrows denote growth-rate coupling via ∂_t in (1). Solid arrows represent couplings between coefficients $D_m^{(j)}$, labelled ×, which contribute to the leading-order $[O(\epsilon\tilde{A}^n)]$ growth-rate calculation, while dashed arrows represent couplings with coefficients $D_m^{(j)}$, labelled ○, which do not.

4. Disturbance growth rate and energy budget

An analysis of higher order in $\tilde{A}$ is required to calculate the disturbance growth rate and energy budget over the resonant surface. Substitution of (4), (5) and (6) into (1) and separating by functional form results in an infinite series of perturbation equations. Each set of five equations can be characterized by an ordered pair (m,j), representing the corresponding powers of $\mathrm{e}^{\mathrm{i}\phi}$ (Floquet index) and $\tilde{A}$, respectively. Since the primary wave fields $\tilde{u}$ and $\tilde{b}$ (equation (2)) comprise terms proportional to $\tilde{A}\,\mathrm{e}^{\pm\mathrm{i}\phi}$, each set of equations relates the dynamic-variable coefficients of $\tilde{A}^j$ to those of $\tilde{A}^{j-1}$ with adjacent Floquet indices. In other words, the primary-wave terms couple $\boldsymbol{D}_m^{(j)}$ to $\boldsymbol{D}_{m-1}^{(j-1)}$ and $\boldsymbol{D}_{m+1}^{(j-1)}$. Figure 4 displays the patterns of couplings among dynamic-variable coefficients for powers of $\tilde{A}$ up to $j=n$, for the first four values of n. Since the Floquet indices of the two dominant $O(\epsilon)$ disturbance components (represented in figure 4 by the × symbols at $(m,j)=(0,0)$ and $(-n,0)$) are separated by n, their interaction with the primary wave comprises n successive couplings. This causes the dimensionless growth rate to be $O(\tilde{A}^n)$; its leading-order calculation requires analysis to be carried out to $O(\epsilon\tilde{A}^n)$. The dynamic-variable coefficients and couplings among them that contribute to the calculation of growth rate are represented by the × symbols and solid arrows in figure 4. The other coefficients and couplings (○ symbols and dashed arrows) do not contribute to this calculation; they do however contribute to frequency shifts and resonant-surface deformations, which we have calculated, but omit here for brevity.

For given n the above discussion leads to two systems of perturbation equations of order $\epsilon\tilde{A}$ up to $\epsilon\tilde{A}^n$: one for the leftward coupling chain in figure 4 from $(m,j)=(0,0)$ to $(-n,n)$, and one for the rightward coupling chain from $(-n,0)$ to $(0,n)$. It can be seen that for even n, the two coupling chains share a common dynamic-variable coefficient $[\boldsymbol{D}_{-n/2}^{(n/2)}]$. This coefficient separates into two additive components, one for each direction. To avoid ambiguity we use separate designations for the contributions to the dynamic-variable coefficients $\boldsymbol{D}_m^{(j)}$: $\boldsymbol{L}_m^{(j)}$ for the contributions from the leftward coupling chain, and $\boldsymbol{R}_m^{(j)}$ for the contributions from the rightward coupling chain. Then

$$\boldsymbol{D}_m^{(j)} = \boldsymbol{L}_m^{(j)} + \boldsymbol{R}_m^{(j)}. \tag{14}$$

The growth-rate equations resulting from this manipulation of (1) can be written as

$$\begin{pmatrix} \boldsymbol{W}_{-1} & & & & \\ \boldsymbol{L} & \boldsymbol{W}_{-2} & & & \\ & \ddots & \ddots & & \\ & & \boldsymbol{L} & \boldsymbol{W}_{1-n} & \\ & & & \boldsymbol{L} & \boldsymbol{W}_{1-n} \end{pmatrix} \begin{pmatrix} \boldsymbol{L}_{-1}^{(1)} \\ \boldsymbol{L}_{-2}^{(2)} \\ \vdots \\ \boldsymbol{L}_{1-n}^{(n-1)} \\ \boldsymbol{L}_{-n}^{(n)} \end{pmatrix} = \begin{pmatrix} -\boldsymbol{L}\boldsymbol{P}_0 \\ 0 \\ \vdots \\ 0 \\ -\boldsymbol{S}\boldsymbol{P}_{-n}\, s_g^{(n)}\, r \end{pmatrix}, \tag{15a}$$

$$\begin{pmatrix} \boldsymbol{W}_{1-n} & & & & \\ \boldsymbol{R} & \boldsymbol{W}_{2-n} & & & \\ & \ddots & \ddots & & \\ & & \boldsymbol{R} & \boldsymbol{W}_{-1} & \\ & & & \boldsymbol{R} & \boldsymbol{W}_{0} \end{pmatrix} \begin{pmatrix} \boldsymbol{R}_{1-n}^{(1)} \\ \boldsymbol{R}_{2-n}^{(2)} \\ \vdots \\ \boldsymbol{R}_{1}^{(n-1)} \\ \boldsymbol{R}_{0}^{(n)} \end{pmatrix} = \begin{pmatrix} -\boldsymbol{R}\boldsymbol{P}_{-n}\, r \\ 0 \\ \vdots \\ 0 \\ -\boldsymbol{S}\boldsymbol{P}_{0}\, s_g^{(n)} \end{pmatrix}, \tag{15b}$$

where $\boldsymbol{P}_0, \boldsymbol{P}_{-n}$ are the $O(\epsilon)$ polarization relations given by (13),

$$\boldsymbol{W}_m = \begin{bmatrix} \mathrm{i}\Omega_m & 0 & 0 & \cos\theta & \mathrm{i}\kappa \\ 0 & \mathrm{i}\Omega_m & 0 & 0 & \mathrm{i}\lambda \\ 0 & 0 & \mathrm{i}\Omega_m & -\sin\theta & \mathrm{i}(\mu+m) \\ -\cos\theta & 0 & \sin\theta & \mathrm{i}\Omega_m & 0 \\ \kappa & \lambda & \mu+m & 0 & 0 \end{bmatrix}, \quad \boldsymbol{S} = \begin{bmatrix} 1 & 0 & 0 & 0 & 0 \\ 0 & 1 & 0 & 0 & 0 \\ 0 & 0 & 1 & 0 & 0 \\ 0 & 0 & 0 & 1 & 0 \\ 0 & 0 & 0 & 0 & 0 \end{bmatrix}, \qquad (16a, b)$$

$$\boldsymbol{L} = \begin{bmatrix} \kappa & 0 & -1 & 0 & 0 \\ 0 & \kappa & 0 & 0 & 0 \\ 0 & 0 & \kappa & 0 & 0 \\ 0 & 0 & \mathrm{i} & \kappa & 0 \\ 0 & 0 & 0 & 0 & 0 \end{bmatrix}, \quad \boldsymbol{R} = \begin{bmatrix} -\kappa & 0 & -1 & 0 & 0 \\ 0 & -\kappa & 0 & 0 & 0 \\ 0 & 0 & -\kappa & 0 & 0 \\ 0 & 0 & -\mathrm{i} & -\kappa & 0 \\ 0 & 0 & 0 & 0 & 0 \end{bmatrix} \qquad (16c, d)$$

are the wave submatrix for the mth element, growth-rate coupling submatrix, and left and right primary-wave coupling submatrices, respectively; Ω_m is given by (8), and $s_g^{(n)}$ is the leading-order growth-rate coefficient $\mathrm{Re}[s^{(n)}]$. Equation (15) gives the growth rate for any order n of resonant instability, as a function of phase elevation angle θ and position on the resonant surface (κ, λ, μ). Details of its solution are given in Appendix B. We note that equations similar to (15) can generally be derived for Floquet systems.

Equation (15) can also be used to obtain an energy budget, which helps to characterize the mechanism of instability. Straightforward manipulation of (1) leads to the following normalization-insensitive equations for the spatially averaged energy budget:

$$f_{KE} = f_{SHR} + f_{VHF}, \quad f_{PE} = f_{BOY} - f_{VHF}, \quad f_{SHR} + f_{BOY} = 1, \qquad (17)$$

where

$$\mathrm{f}_{\mathrm{KE}} = [\langle \mathrm{KE} \rangle / \langle \mathrm{TE} \rangle], \quad f_{PE} = [\langle \mathrm{PE} \rangle / \langle \mathrm{TE} \rangle], \quad \mathrm{f}_{\mathrm{SHR}} = \langle \mathrm{SHR} \rangle / [2 s_r \langle \mathrm{TE} \rangle],$$

$$f_{VHF} = \langle \mathrm{VHF} \rangle / [2 s_r \langle \mathrm{TE} \rangle], \quad f_{BOY} = \langle \mathrm{BOY} \rangle / [2 s_r \langle \mathrm{TE} \rangle],$$

$\langle\ \rangle$ represents spatial average,

$$\mathrm{KE} = (u^2 + v^2 + w^2)/2, \quad \mathrm{PE} = b^2/2, \quad \mathrm{TE} = \mathrm{KE} + \mathrm{PE}, \qquad (18)$$

$$\mathrm{SHR} = -\partial_\eta \tilde{u}(uw), \quad \mathrm{VHF} = -\cos\theta(bu) + \sin\theta(bw), \quad \mathrm{BOY} = -\partial_\eta \tilde{b}(bw), \qquad (19)$$

and all disturbance quantities are now the real parts of their earlier counterparts. Then f_{KE} and f_{PE} are the proportions of disturbance kinetic and potential energy, f_{SHR} and f_{BOY} represent the relative importance of shear conversion and buoyancy conversion in the extraction of primary-wave energy, and f_{VHF} represents the relative vertical heat flux. While f_{KE} and f_{PE} are constrained to be between 0 and 1, f_{SHR}, f_{VHF}, and f_{BOY} are not.

For small $\tilde{A}$, $\langle \mathrm{KE} \rangle$ and $\langle \mathrm{PE} \rangle$ are $O(\epsilon^2)$, $\langle \mathrm{SHR} \rangle$, $\langle \mathrm{VHF} \rangle$, $\langle \mathrm{BOY} \rangle$ are $O(\epsilon^2 \tilde{A}^n)$, and $s_r = O(\tilde{A}^n)$, so that all the fractional quantities are $O(1)$. There are lower-order terms in the equations for SHR, VHF, and BOY, but they do not contribute to the spatial averages. Calculation of the leading-order $\langle \mathrm{KE} \rangle$ and $\langle \mathrm{PE} \rangle$ requires only the $O(\epsilon)$ solution. Calculation of the leading-order $\langle \mathrm{SHR} \rangle$ and $\langle \mathrm{BOY} \rangle$ requires solutions of $O(\epsilon)$ up to $O(\epsilon \tilde{A}^{n-1})$. The direct calculation of $\langle \mathrm{VHF} \rangle$ requires a higher-order solution; however, it can be obtained indirectly from the energy-budget equations (17). As noted by Yeh & Liu (1981) for $n = 1$, equipartition of energy

$$f_{KE} = f_{PE} = 0.5 \qquad (20)$$

applies to resonant interactions involving only internal-gravity-wave components,

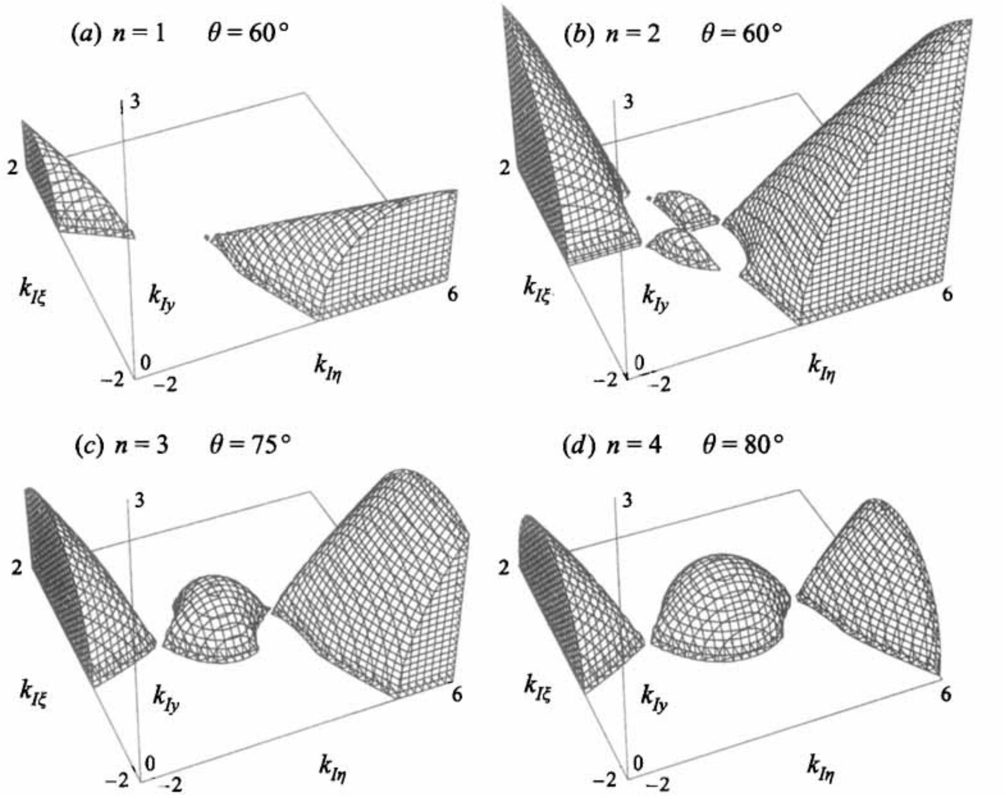

FIGURE 5. Resonant-sum surfaces for the first four resonant orders n, for selected primary-wave phase elevation angles θ. $-k_{Iy}$ is also a solution; this reflection is not shown. The solution shown does not vary with echo number; for the chosen echo, $k_{I\xi} = \kappa$, $k_{I\eta} = \mu$, $k_{Iy} = \lambda$. The primary wavenumber is $\tilde{\boldsymbol{k}} = \hat{\boldsymbol{e}}_\eta$, and the other disturbance wavenumber is $\boldsymbol{k}_{II} = n\tilde{\boldsymbol{k}} - \boldsymbol{k}_I$.

because it applies to internal gravity waves individually. The leading-order non-cancelling terms in the calculation of ⟨SHR⟩ and ⟨BOY⟩ are

$$\langle \mathrm{SHR} \rangle = \frac{\epsilon^2 \tilde{A}_n}{2} \sum_{m=0}^{n-1} \mathrm{Re}\,[u_{-m}^{(m)} w_{-m-1}^{(n-1-m)*} + u_{-m-1}^{(n-1-m)} w_{-m}^{(m)*}] + O(\epsilon^2 \tilde{A}^{n+1}), \qquad (21a)$$

$$\langle \mathrm{BOY} \rangle = \frac{\epsilon^2 \tilde{A}^n}{2} \sum_{m=0}^{n-1} \mathrm{Im}\,[b_{-m}^{(m)} w_{-m-1}^{(n-1-m)*} - b_{-m-1}^{(n-1-m)} w_{-m}^{(m)*}] + O(\epsilon^2 \tilde{A}^{n+1}), \qquad (21b)$$

where $u_{m}^{(j)}$, $w_{m}^{(j)}$, and $b_{m}^{(j)}$ are components of $\boldsymbol{L}_{m}^{(j)}$ and $\boldsymbol{R}_{m}^{(j)}$ (equations (4), (14)), as calculated from (15). Equations (21) will be used in §7 to characterize the energy transfer.

5. Three-dimensional disturbances

Examples of resonant-sum surfaces in wavenumber space of one of the two disturbance components are displayed in figure 5 for the first four orders of resonance n, and the corresponding frequencies are displayed in figure 6. $s_i^{(0)}$ can be recovered using (8) with $m = 0$ and $\Omega_0 = -\omega_I$. The two-dimensional $n = 1$ resonant solutions ($\lambda = 0$ perimeters in figures 5a and 6a) were first produced by Phillips (1966). We can use these figures to investigate the existence of wave-shear-aligned resonant instabilities. Since the gravity-wave shear flow is directed along the ξ-axis, these have $\kappa = 0$ (i.e.

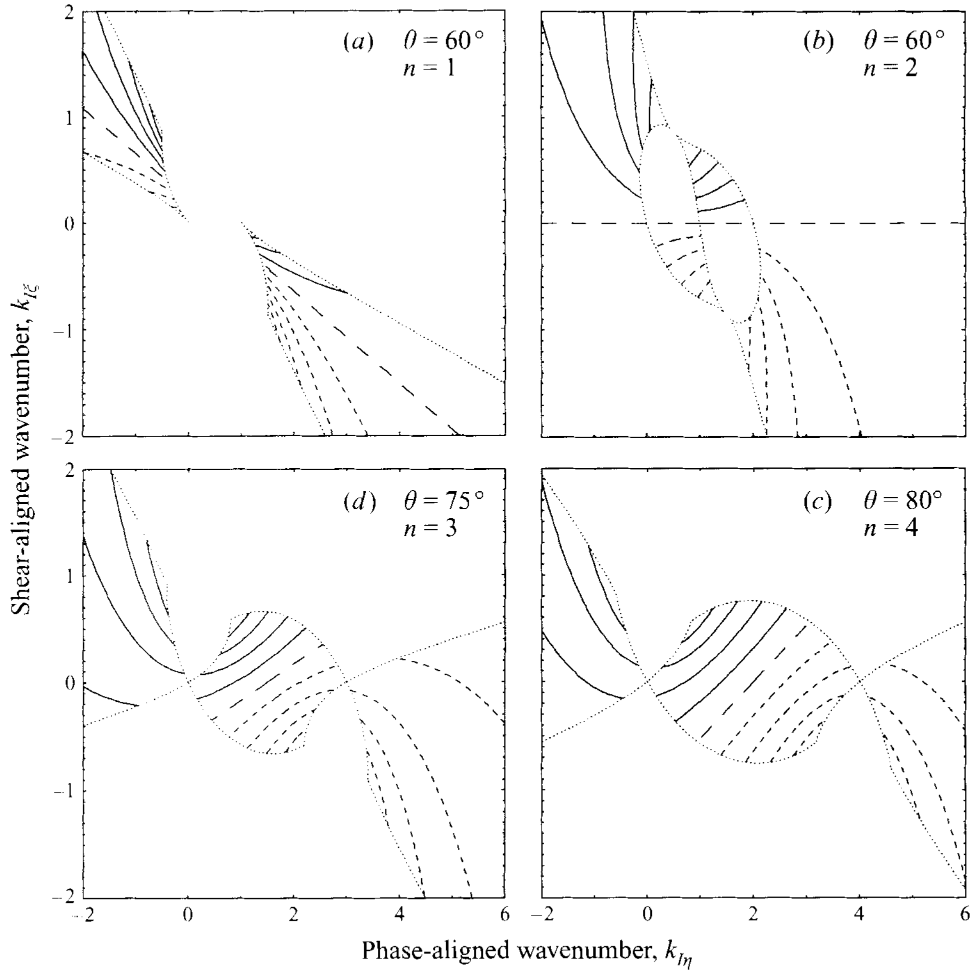

FIGURE 6. Contours of disturbance-component frequency ratio $\omega_I/n\tilde{\omega}$ over the resonant surfaces shown in figure 5. Long-dash curves represent $\omega_I/n\tilde{\omega} = 1/2$; solid (short-dash) curves represent progressively larger (smaller) values, with linear increment 0.1. Primary-wave frequency is $\tilde{\omega} = \cos\theta$; the other disturbance component frequency is $\omega_{II} = n\tilde{\omega} - \omega_I$.

$k_{I\xi} = k_{II\xi} = 0$ for the two components of resonant instability). As seen in figures 5(*a*) and 6(*a*), the $n = 1$ resonant-sum surface does not cross the $k_{I\xi} = 0$ plane; therefore, as noted in the Introduction, there are no $n = 1$ shear-aligned instabilities. The $n = 2$ surface in figure 5(*b*) just touches the $k_{I\xi} = 0$ plane; however, we have found that the disturbance is always neutrally stable there. This is the case at all phase elevation angles θ. In contrast, the $n = 3$, 4 surfaces in figures 5(*c*) and 5(*d*) cross the $k_{I\xi} = 0$ plane at all $k_{I\eta} = \mu$ values, and we have found positive growth rates there. This holds for all $n \geqslant 3$ and all θ satisfying (12). Therefore, higher-order resonant instabilities with $n \geqslant 3$ include growing shear-aligned instabilities. The $n \geqslant 3$ resonant surfaces (e.g. figures 5*c* and 5*d*) all contain a central shear-aligned point, $k_{I\eta}(= \mu) = n/2$, $k_{I\xi} = 0$, at which the frequencies of the two components both equal $n\tilde{\omega}/2$ (figures 6*c* and 6*d*); this point of symmetry will be shown to be the preferred shear-aligned disturbance in §7.

Results for the range $-90° < \theta < 0$, corresponding to upward energy propagation, are easily recovered using the symmetry of the equations, as follows:

$$(\theta, \kappa) \to (-\theta, -\kappa), \quad (u_m, v_m, w_m, b_m, p_m) \to (-1)^m(-u_m, v_m, w_m, -b_m, p_m). \quad (22)$$

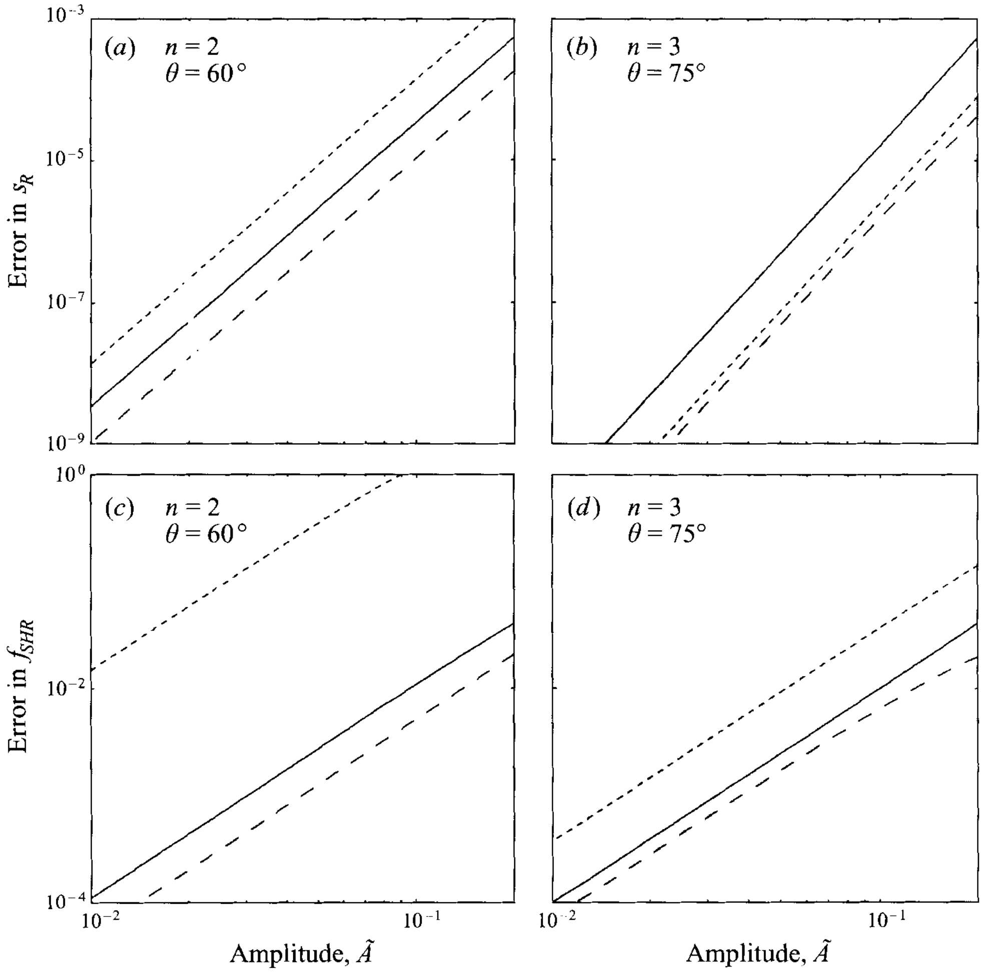

FIGURE 7. Verification of small-$\tilde{A}$ equations at various points on the $n = 2$ and 3 resonant surfaces. We compare s_r and f_{SHR} from exact finite-$\tilde{A}$ calculations, to $s_g^{(n)} \tilde{A}^n$ and $\langle \mathrm{SHR} \rangle / 2 s_g^{(n)} \tilde{A}^n$, from (15) and (21 *a*) for three different values of (κ, μ). For $n = 2$ these are solid $(0.5, -2)$, short dash $(1, -1)$, long dash $(0.55, 1.1)$; for $n = 3$ these are solid $(0, 1.5)$, short dash $(0.3, 1.8)$, long dash $(0.1, 4.2)$; λ is chosen on the resonant surface. Slopes for s_r error approach 4 ($n = 2$) and 5 ($n = 3$); slopes for f_{SHR} error approach 2.

This transformation leaves the time dependence and energy budget unchanged. Thus, the physically important characteristics of the instability do not depend on whether the phase progression is upward or downward. Also note that λ appears in the resonant equation (11) only as λ^2; therefore $-\lambda$ is also a solution.

Figure 7 provides numerical verification of the small-$\tilde{A}$ analysis of §4. The curves shown were obtained by comparing the predicted leading-order resonant growth rates (15) and energy budget (21) to exact numerical solutions of the original equations (1) over a range of finite but small $\tilde{A}$, at various locations on the resonant surface, for two different resonant orders ($n = 2, 3$). The procedures used to solve (15) are described in Appendix B; equation (21) is then evaluated directly. The eigenvalue procedure used to obtain exact finite-$\tilde{A}$ numerical solutions of (1) is described in §2. The linearity of the curves in the small-$\tilde{A}$ region indicates power-law dependence for errors in the

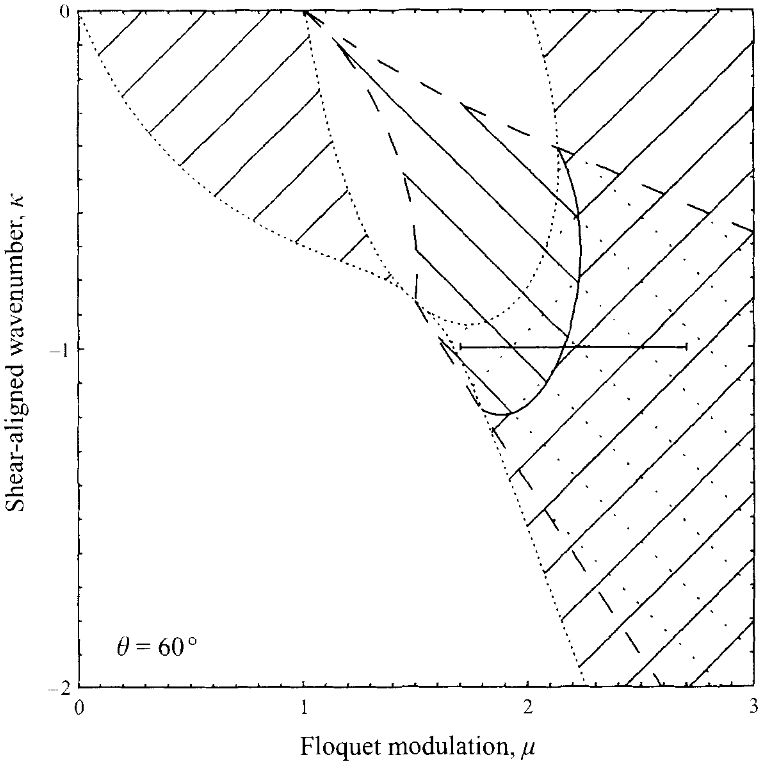

FIGURE 8. Expanded view of an $M = 3$ curve (solid curve), which is the intersection of two $M = 2$ resonant surfaces ($n = 1, 2$). Long-dash (dotted) curves bound the $n = 1$ (2) surface projection, which is hatched by diagonal lines with negative (positive) slope; where both exist, the lines of the hidden surface are dotted. The horizontal segment indicates the cross-section investigated in figures 9 and 10.

resonant solutions. The limiting slopes of these curves show that at the chosen locations, our equations are correct to at least the expected orders in $\tilde{A}$.

Presentation of the growth rates over the resonant surfaces is hampered by the appearance of curves on which $s_r^{(n)} = \infty$; for given n, there are $n-1$ such curves. This represents an apparent difficulty for this theory that will be resolved in the next Section.

6. Interactions involving more than two disturbance components ($M > 2$)

Recall that at the beginning of §3, we made an assumption restricting the number of non-vanishing disturbance components that survive as $\tilde{A} \rightarrow 0$ to the value $M = 2$. The $s_r^{(n)} = \infty$ contours described above are precisely those locations in (κ, λ, μ) space at which more than two elements in the Floquet sum do not vanish as $\tilde{A} \rightarrow 0$, in violation of the $M = 2$ assumption. On these curves, one of the Floquet elements (equation (5)) between $-n$ and 0 has a frequency (equation (8)) that satisfies the gravity-wave dispersion relation. This creates a linear dependence in the corresponding $\boldsymbol{W}_m$ submatrix in (15). Thus the result $s_r^{(n)} = \infty$ arises because $s_r^{(n)} \tilde{A}^n$ is an inappropriate functional representation of the true growth rate s_r, which is finite. We will show that in the vicinity of these curves, the solution undergoes an order transition to a solution with lower-order growth rate; in this sense $s_r^{(n)} = \infty$ is as faithful a representation of the solution as can be obtained using the functional representation that follows from the violated $M = 2$ assumption.

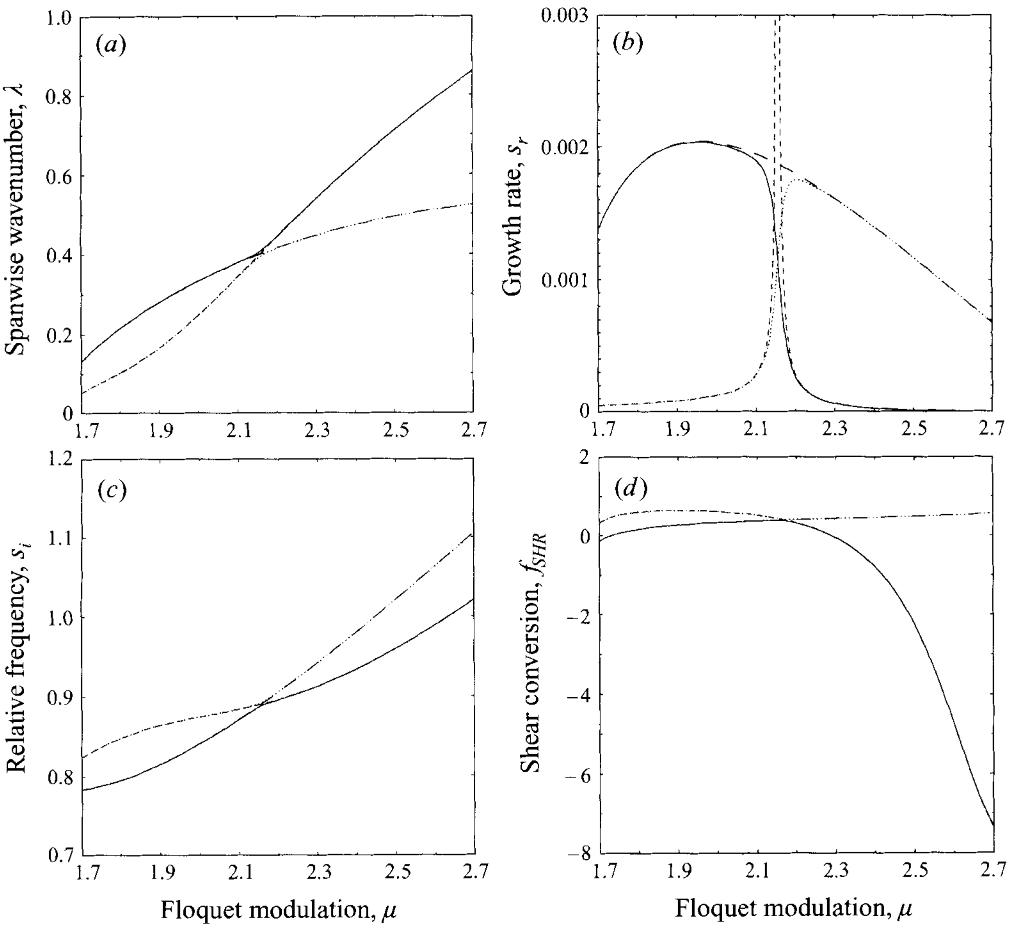

FIGURE 9. Case study of the breakdown of the small-$\tilde{A}$ resonant equations where the $M = 2$ assumption is violated. The resonant $n = 1$ (long-dash) and $n = 2$ (short-dash) solutions are compared to exact finite-$\tilde{A}$ solutions of (1), with $\tilde{A} = 0.01$, along the $\kappa = -1$ cut shown in figure 8. Solid (dotted) curves represent the finite-$\tilde{A}$ ridgetop (see figure 10a and text) solution starting near the $n = 1$ (2) solution at $\mu = 1.7$ and moving rightward. The direction of motion in μ does not affect the result.

Each disturbance component that participates in the interaction introduces another dispersion relation that must be satisfied. No matter how many components participate, there is only one free parameter for given (κ, λ, μ): $s_i^{(0)}$. Thus, in (κ, λ, μ)-space, $M = 2$ interactions occupy two-dimensional surfaces (as shown in figure 5); $M = 3$ interactions occupy curves (the $s_r^{(n)} = \infty$ curves of present interest); $M = 4$ interactions occupy isolated points (where two $s_r^{(n)} = \infty$ contours cross); and $M > 4$ interactions cannot occur except at particular values of phase elevation angle θ.

The $M = 3$ curves discussed above also represent the intersection curves of two $M = 2$ surfaces. Here three Floquet elements, instead of two, satisfy the gravity-wave dispersion relation and thus have non-zero coefficients as $\tilde{A} \to 0$. These three elements allow three pairs, each of which can resonate with the primary wave. However, only two of the three interactions are unstable sum interactions; the other is necessarily a neutrally stable difference interaction. As an example, we focus on the intersection of the $\theta = 60°$, $n = 2$ surface in figure 5(b) with the $\theta = 60°$, $n = 1$ surface in figure 5(a).

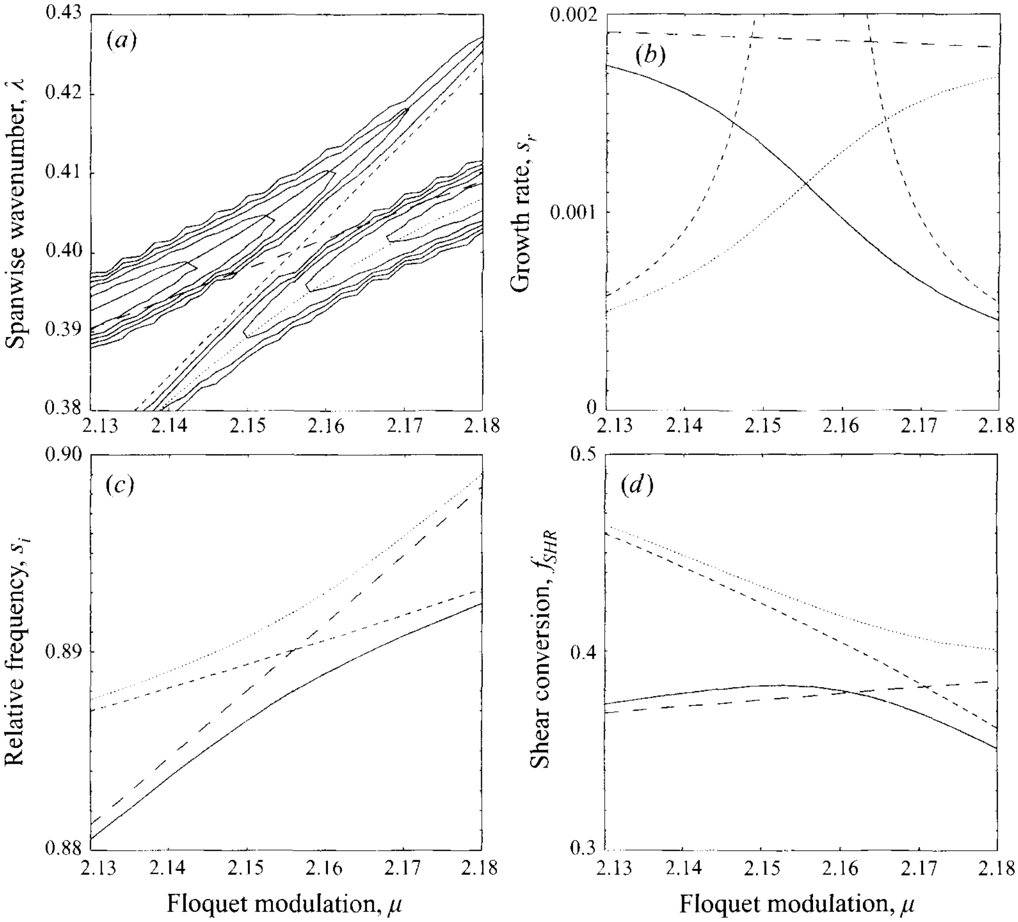

FIGURE 10. Expanded view of figure 9 in the region near the $M = 3$ intersection. Frame (*a*) also shows superimposed growth-rate contours from the exact finite-$\tilde{A}$ solutions, which illustrate the ridgelike nature of the resonances, and the order transition.

Figure 8 shows an expanded view of this intersection. In the vicinity of the intersection, both $M = 2$ solutions from §4 break down.

In order to examine the true solution in this region, we turn to exact solutions of the original disturbance equations (1) at finite but small $\tilde{A}$, along a $\kappa = -1$ cut that passes through the intersection, as indicated in figure 8. Figure 9 compares exact finite-$\tilde{A}$ solutions (for $\tilde{A} = 0.01$) to the $M = 2$ resonant-sum solutions. It can be seen that the two agree well, except near the intersection point where the $M = 2$ assumption fails. This provides verification of (15) for $n = 1$ and 2, as well as an indication of the nature of the failure of the $M = 2$ solutions where the assumptions are violated.

Figure 10 provides a closeup view of the solutions in the region of the intersection. Figure 10(*a*) includes exact finite-$\tilde{A}$ s_r contours showing resonance broadening due to finite amplitude. There are two non-intersecting finite-$\tilde{A}$ ridges, on contrast to the $M = 2$ prediction that the $n = 1, 2$ resonant surfaces cross. Furthermore, in progressing along either ridgetop past the $M = 2$ intersection, there is a continuous transition from one order to the other. In the vicinity of the intersection, there are three dominant Floquet elements. Moving away from the intersection in one direction, one element decays, leaving an $n = 1$ triad; moving in the other direction, a different element decays,

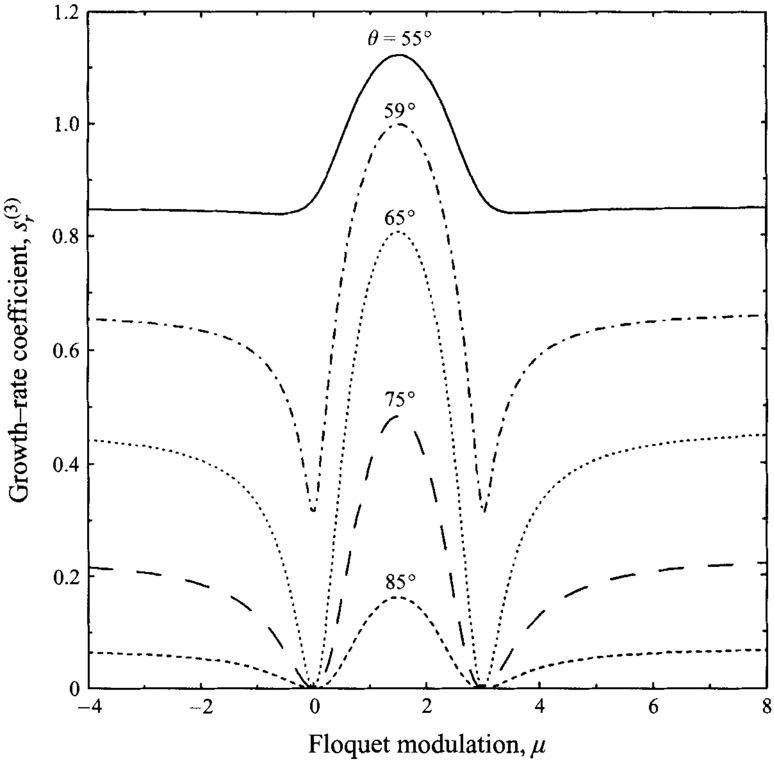

FIGURE 11. Growth-rate coefficient $s_r^{(3)}$ for the lowest-order ($n = 3$) shear-aligned instability, as a function of Floquet modulation μ for various primary-wave phase elevation angles θ.

leaving an $n = 2$ interaction. This indicates that the two portions of the $n = 2$ resonant surface on either side of the intersection curve in figure 8 do not connect to each other, and likewise for the two portions of the $n = 1$ surface. Instead, each undergoes an order transition to connect to one of the surface portions of the other order. This means that the various orders of resonant interactions connect to one another even in the limit $\tilde{A} \rightarrow 0$. We have verified that this coalescence is not a spurious effect associated with roundoff amplification in the eigenvalue algorithm and/or validity of the Floquet form of solution.

No additional growing solution appears in the vicinity of the intersection curve, which is also an $M = 3$ resonant curve. This means that interactions involving three infinitesimal disturbance waves and the primary wave do not form a distinct linearly independent family of solutions, but rather link together two $M = 2$ solutions of different order where the $M = 2$ resonant surfaces appear to intersect. Near this intersection both $M = 2$ solutions break down, while the true solutions each undergo order transitions as they cross over.

7. Shear-aligned disturbances

Now that we have identified the regions in disturbance (κ, λ, μ)-space in which $M = 2$ theory breaks down, we are free to examine the solutions elsewhere. We now consider wave-shear-aligned disturbances. As pointed out in § 5, the lowest-order shear-aligned resonant instabilities are of order $n = 3$. These exist for $\theta \geqslant \cos^{-1}(2/3) \simeq 48°$ (equation (12)). The $n = 3$ growth-rate plots in figure 11 show that the central

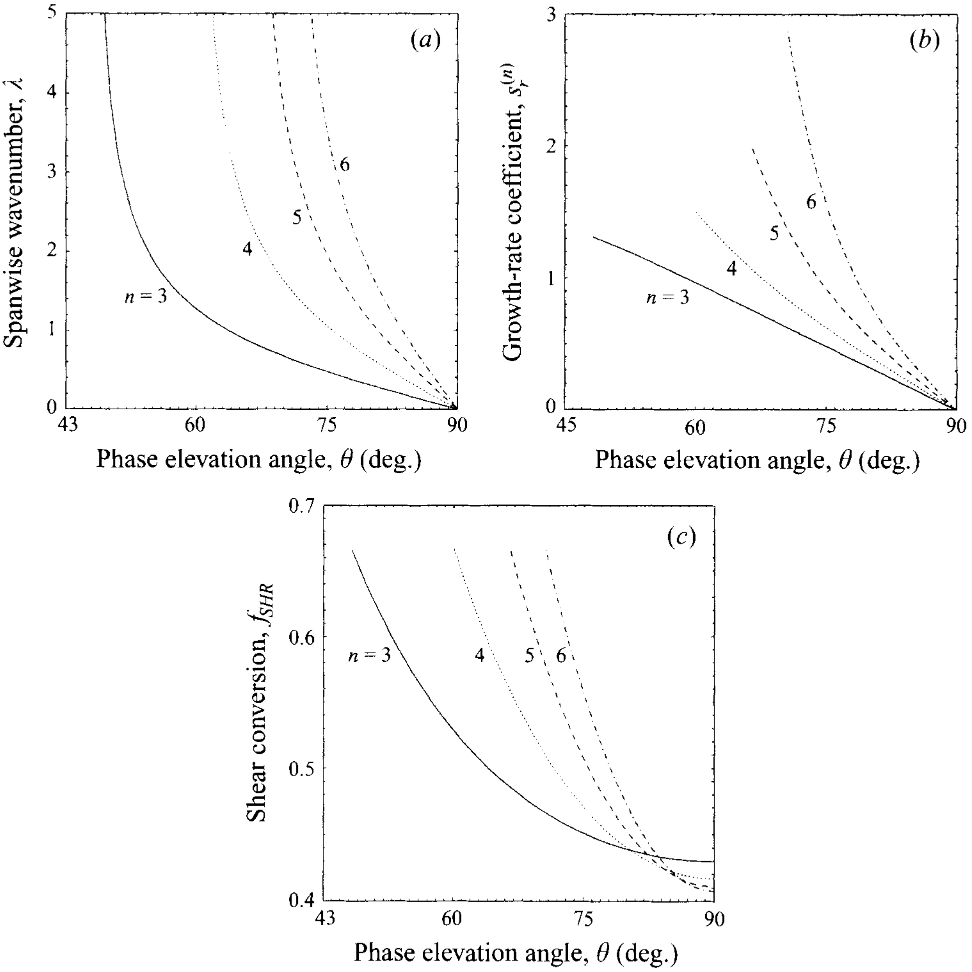

FIGURE 12. Characteristics of the first four orders ($n = 3$, 4, 5, 6) of shear-aligned instability, as function of θ. Two-period modulation (half-integer μ) is preferred by $n = 3, 5$; single-period modulation (integer μ) is preferred by $n = 4, 6$. All prefer zero relative frequency. Disturbance energy is equally partitioned between kinetic and potential.

symmetry point, $\mu = 1.5$, is the preferred Floquet modulation among shear-aligned disturbances for all phase elevation angles. This point is never on or near an $M = 3$ curve for any θ, so the $M = 2$ solution is valid there. The echo solutions have peak μ displaced by integer values, but all have a lowest denominator of 2. This means that the lowest-order shear-aligned resonant instability prefers subharmonic modulation. These preferred solutions also have $s_i^{(0)} = 0$, and so are stationary with respect to wave phase. Similar results hold for even higher orders, except that the even orders prefer single-period modulation (integer μ values).

Figure 12 displays the small-$\tilde{A}$ characteristics of the preferred $n = 3, 4, 5$ and 6 shear-aligned resonant instabilities, as functions of phase elevation angle θ. For each n, as θ increases from $\cos^{-1}(2/n)$ (equation (12)), preferred spanwise wavenumber (*a*) decreases monotonically from ∞, while the growth rate coefficient (*b*) decreases monotonically. (Note that growth-rate coefficients of different orders are not comparable, because the functional form of growth rate $s_r^{(n)}\tilde{A}^n$ varies with n.) Disturbance energy extraction (*c*) changes from dominantly shear conversion to dominantly buoyancy conversion, but

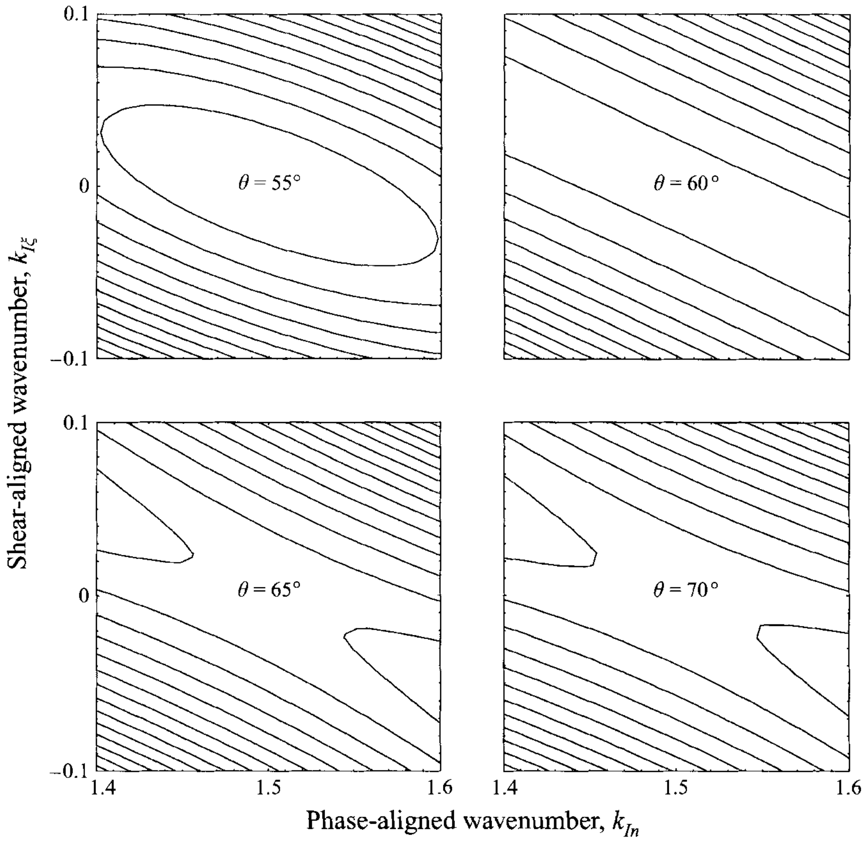

FIGURE 13. Contour patterns of growth-rate coefficient $s_r^{(3)}$ near the shear-aligned maximum, obtained from (15), for a variety of primary-wave phase elevation angles θ.

stays within a fairly narrow band throughout. These shear-aligned instabilities convert potential energy of the primary wave into disturbance kinetic energy, even though the wave amplitude is too small to cause overturning of isentropes. This conversion is possible because the isentropes are not horizontal. Similar reasoning explains the absence of threshold amplitude for slantwise static instability (Hines 1971, 1988).

Although $\mu = 1.5$ is the preferred $n = 3$ shear-aligned disturbance for all primary-wave phase elevation angles θ, this point is not always a two-dimensional growth-rate maximum on the resonant surface; for $\theta > 60°$, it is a saddlepoint. This effect is illustrated in figure 13. This raises the possibility that an oblique, rather than strictly shear-aligned, orientation is preferred for some θ. Further investigation of this effect using the present small-$\tilde{A}$ $M = 2$ analysis is hampered by the presence of $M = 3$ intersections, near which $M = 2$ theory breaks down. Therefore, we postpone the detailed analysis of oblique disturbances to a future paper on finite-amplitude waves, using a method that does not share this difficulty.

8. Conclusions

We have presented a theory for treating resonant temporal instabilities of a primary wave. The linear formulation offers some advantages over the traditional weakly nonlinear formulation, including a simplified treatment of higher-order resonances.

Our technique can, in principle, be applied to any small-amplitude fluid wave motion. In this paper, we have applied it to internal gravity waves, with the following main results:

(i) We have calculated the wavenumbers, frequencies, growth rates, and energy budgets for higher-order resonant instabilities of small-amplitude internal gravity waves, that reduce to two wave components satisfying $\omega_I + \omega_{II} = n\tilde{\omega}$, $\boldsymbol{k}_I + \boldsymbol{k}_{II} = n\tilde{\boldsymbol{k}}$.

(ii) Only higher-order resonant instabilities with $n \geqslant 3$ can align with the wave shear flow; these are restricted to waves with frequency below $2N/n$. The preferred shear-aligned instability corresponds to a symmetry in the resonant surface, for which both dominant components have frequency $n\tilde{\omega}/2$ at all wave frequencies $\tilde{\omega}$. Here, the disturbance is stationary with respect to wave phase; odd-n resonances prefer two-period modulation in wave phase, and even-n resonances prefer single-period modulation. They can convert wave potential energy into kinetic energy, even in the limit of small wave amplitude, in which isentropes are not vertically overturned.

(iii) The various orders of resonant interaction connect to each other in disturbance-wavenumber space. Near the intersection curve of their resonant surfaces, two solutions of different order undergo order transitions to 'switch over' to each other.

(iv) Interactions involving three or more distinct infinitesimal components and one finite primary wave (participating in the resonance one or more times) are not distinct classes of solutions. Instead, they represent the order transitions referred to above.

We are grateful to Lin Zhong, A. H. Manson, C. E. Meek, and N. Gavrilov for valuable discussions, and to I. Oznovich for advice on presentation. Thanks are due to the Canadian Network for Space Research for providing computing facilities. L. J. S. was supported by a Natural Sciences and Engineering Research Council of Canada postdoctoral fellowship. This work was partially supported by an NSERC Operating Grant and by the Atmospheric Environment Service of Canada.

Appendix A

The freely propagating wave equations ((1), (2) with $\tilde{A} = 0$) allow two types of natural modes: gravity wave and vortical. Pure vortical motion involves steady unidirectional horizontal flow whose amplitude varies over a plane normal to the flow direction; such motion carries vertical vorticity. The vortical dispersion relation is $\omega = 0$, whence it follows that two vortical modes cannot resonate with a primary gravity wave. Dong & Yeh (1988) proposed a non-resonant vortical-pair instability that exists only for $\tilde{A} > (\sqrt{2}\sin\theta)^{-1}$; we cannot investigate this instability and possible higher-order counterparts in the context of the present analysis because the proposed critical amplitude is too large for small-$\tilde{A}$ theory. This leaves two possible arrangements for the disturbance pair: one gravity wave plus one vortical mode, and two gravity waves. Any sum interaction involving one gravity wave plus one vortical mode is simultaneously a difference interaction. We have verified numerically the implication that this combination cannot constitute a growing disturbance in the limit of small $\tilde{A}$. Thus, all growing $M = 2$ resonant interactions allowed by (1) involve three gravity waves.

Compressible equations would allow disturbance pairs in which one or both of the components are acoustic modes. Since for any gravity wave $\tilde{\omega} < \omega_a$, the acoustic cutoff frequency, resonance involving acoustic modes must be higher-order; the two arrangements above require $n > \omega_a/\tilde{\omega}$ and $n > 2\omega_a/\tilde{\omega}$ respectively. We have not investigated these acoustic resonances, as it is not clear that they are of atmospheric or oceanic importance.

Compressibility also plays a secondary role in the high-frequency region of the atmospheric gravity-wave branch. This means that atmospheric application of (1) and (2) is restricted to primary-wave vertical wavelengths that are not large compared to the density scale height. In addition, disturbance solutions near the curves in wavenumber space on which $\omega_I = 1$ or $\omega_{II} = 1$ depart slightly from their physical (acoustic–gravity wave) counterparts. We note that compressible effects cannot easily be incorporated into finite-$\tilde{A}$ calculations, because the linear primary-wave solution is no longer a solution of the nonlinear equations.

We have also neglected effects of rotation. Therefore, solutions near the curves in wavenumber space on which $\omega_I = 0$ and $\omega_{II} = 0$ (discontinuities in figure 5) depart from their physical counterparts. These discontinuities are located at

$$(\mu, \kappa) = (n\cos^2\theta \pm Q\sin\theta,\ n\cos\theta\sin\theta \mp Q\cos\theta)$$

and $(\mu, \kappa) = (n\sin^2\theta \pm Q\sin\theta, -n\cos\theta\sin\theta \mp Q\cos\theta)$, where $Q = (1-n^2\cos^2\theta)^{1/2}$.

Appendix B

We solve the growth-rate equations, (15), as follows. The set of $10n$ equations (5 dynamic variables × 2 coupling chains × n steps in each chain) therein has $10n+2$ unknowns: $\boldsymbol{L}_{-1}^{(1)}, \ldots, \boldsymbol{L}_{-n}^{(n)}, \boldsymbol{R}_{1-n}^{(1)}, \ldots, \boldsymbol{R}_0^{(n)}, s_g^{(n)}$, and r. The latter two unknowns appear as a product in the last element on the right-hand side of (15a). This nonlinearity is removed by dividing (15b) by r, leaving the two variables $s_g^{(n)} r$ and $s_g^{(n)}/r$ on the right-hand side. The underdetermination (two less equations than variables) implies that the solution space of (15) is a two-dimensional surface in $10n+2$ dimensional space, rather than a single point. However, the variation from one solution to another is entirely confined to the highest-order (in $\tilde{A}$) subvectors $\boldsymbol{L}_{-n}^{(n)}$ and $\boldsymbol{R}_0^{(n)}$, as follows. The two submatrices W_{-n} and W_0 each contain a single linear dependence, because Ω_0 and Ω_{-n} satisfy their respective dispersion relations, and the resonance condition, owing to the assumption that (κ, λ, μ) is on the resonant surface. Therefore, the addition of any wave solution to $\boldsymbol{L}_{-n}^{(n)}$ or $\boldsymbol{R}_0^{(n)}$ (i.e. solution of $\mathsf{W}_0 \boldsymbol{R}_0^{(n)} = 0$ or $\mathsf{W}_{-n} \boldsymbol{L}_{-n}^{(n)} = 0$) does not affect the right-hand side. Because of this, the variables of greater interest $-s_g^{(n)}, r$, and the lower orders (in $\tilde{A}$) of $\boldsymbol{L}_m^{(j)}$ and $\boldsymbol{R}_m^{(j)}$, for $j = 1, \ldots, n-1$, are independent of such additions; they are uniquely determined. This allows us to assign one of the five elements (e.g. pressure or buoyancy) in each of $\boldsymbol{L}_{-n}^{(n)}$ and $\boldsymbol{R}_0^{(n)}$, and still solve for the uniquely determined variables. The result is a system of $10n$ linear equations in $10n$ variables. For each chosen n, θ, and parameter set (κ, λ, μ) on the resonant surface, we solve this system efficiently as a series of 5 × 5 matrix equations, to obtain $\boldsymbol{L}_{-1}^{(1)}, \ldots, \boldsymbol{L}_{-n}^{(n)}$, $\boldsymbol{R}_{1-n}^{(1)}/r, \ldots, \boldsymbol{R}_0^{(n)}/r$, $s_g^{(n)} r$, and $s_g^{(n)}/r$, with $\boldsymbol{L}_{-n}^{(n)}$ and $\boldsymbol{R}_0^{(n)}$ undetermined to a multiple of their respective wave solutions. Then $s_g^{(n)}$ and r are recovered from $s_g^{(n)} r$ and $s_g^{(n)}/r$. Our calculation always results in $s_g^{(n)}$ being purely real and r being either purely real or purely imaginary. Finally, $\boldsymbol{R}_{1-n}^{(1)}, \ldots, \boldsymbol{R}_0^{(n)}$ are recovered from $\boldsymbol{R}_{1-n}^{(1)}/r, \ldots, \boldsymbol{R}_0^{(n)}/r$ and r.

REFERENCES

CLEVER, R. M. & BUSSE, F. H. 1977 Instabilities of longitudinal convection rolls in an inclined layer. *J. Fluid Mech.* **81**, 107–127.

CRAIK, A. D. D. 1985 *Wave Interactions and Fluid Flows.* Cambridge University Press.

DONG, B. & YEH, K. C. 1988 Resonant and nonresonant wave–wave interactions in an isothermal atmosphere. *J. Geophys. Res.* **93**, 3729–3744.

DRAZIN, P. G. 1977 On the instability of an internal gravity wave. *Proc. R. Soc. Lond.* A **356**, 411–432.

FRITTS, D. C., ISLER, J. R. & ANDREASSEN, O. 1994 Gravity wave breaking in two and three dimensions, 2, Three-dimensional evolution and instability structure. *J. Geophys. Res.* **99**, 8109–8213.

FRITTS, D. C., ISLER, J. R. & THOMAS, G. E. 1993 Wave breaking signatures in noctilucent clouds. *Geophys. Res. Lett.* **20**, 2039–2042.

HASSELMANN, K. 1967 A criterion for nonlinear wave stability. *J. Fluid Mech.* **30**, 737–739.

HINES, C. O. 1971 Generalizations of the Richardson criterion for the onset of atmospheric turbulence. *Q. J. R. Met. Soc.* **97**, 429–439.

HINES, C. O. 1988 Generation of turbulence by atmospheric gravity waves. *J. Atmos. Sci.* **45**, 1269–1278.

KELLY, R. E. 1977 The onset and development of Rayleigh–Benard convection in shear flows: a review. *Physiochemical Hydrodynamics*, Vol. 1 (ed. V. G. Levich). London: Advance Publications.

KLAASSEN, G. P. & PELTIER, W. R. 1985 The onset of turbulence in finite amplitude Kelvin–Helmholtz billows. *J. Fluid Mech.* **155**, 1–35.

KLAASSEN, G. P. & PELTIER, W. R. 1991 The influence of stratification on secondary instability in free shear layers. *J. Fluid Mech.* **227**, 71–106.

KLOSTERMEYER, J. 1982 On parametric instabilities of finite-amplitude internal gravity waves. *J. Fluid Mech.* **119**, 367–377.

MCINTYRE, M. E. 1989 On dynamics and transport near the polar mesopause in summer. *J. Geophys. Res.* **94**, 14617–14628.

MCLEAN, J. W. 1982 Instabilities of finite-amplitude water waves. *J. Fluid Mech.* **114**, 315–341.

MIED, R. P. 1976 The occurrence of parametric instabilities in finite-amplitude internal gravity waves. *J. Fluid Mech.* **78**, 763–784.

PHILLIPS, O. M. 1960 On the dynamics of unsteady gravity waves of finite amplitude. Part 1. *J. Fluid Mech.* **9**, 193–217.

PHILLIPS, O. M. 1966 *The Dynamics of the Upper Ocean.* Cambridge University Press.

THORPE, S. A. 1994 The stability of statically unstable layers. *J. Fluid Mech.* **260**, 315–331.

WINTERS, K. B. & D'ASARO, E. A. 1994 Three-dimensional wave instability near a critical level. *J. Fluid Mech.* **272**, 255–284.

WINTERS, K. B. & RILEY, J. J. 1992 Instability of internal waves near a critical level. *Dyn. Atmos. Oceans* **16**, 249–278.

YEH, K. C. & LIU, C. H. 1981 The instability of atmospheric gravity waves through wave–wave interactions. *J. Geophys. Res.* **86**, 9722–9728.

ZAKHAROV, V. E. 1968 Stability of periodic waves of finite amplitude on the surface of a deep fluid. *J. Appl. Mech. Tech. Phys.* **2**, 190–194.